



Characterisation of $\text{Pb}_2\text{Rh}_2\text{O}_7$ and $\text{Y}_2\text{Rh}_2\text{O}_7$: An unusual case of pyrochlore stabilisation under high pressure, high temperature synthesis conditions

Journal:	<i>Journal of Materials Chemistry C</i>
Manuscript ID	TC-ART-11-2023-004389.R1
Article Type:	Paper
Date Submitted by the Author:	11-Jan-2024
Complete List of Authors:	Injac, Sean; Kyoto University, Institute for Chemical Research; The University of Edinburgh School of Chemistry, Centre for Science at Extreme Conditions Mullens, Bryce; University of Sydney, Chemistry Denis-Romero, Fabio ; Kyoto University, Institute for Chemical Research; Institut NEEL, Materials Avdeev, Maxim; Australian Nuclear Science and Technology Organisation, Barnett, Christopher; The University of Sydney Faculty of Science, Yuen, Alexander; University Of Sydney, School of Chemistry; The University of Sydney Amano-Patino, Midori; Kyoto University, Institute for Chemical Research; Institut NEEL Mukherjee, Supratik; Advanced Center of Research in High Energy Materials (ACRHEM), University of Hyderabad, Physics Vaitheeswaran, Ganapathy; University of Hyderabad Singh, David Joseph; University of Missouri, Department of Physics and Astronomy Kennedy, Brendan; University of Sydney, Chemistry Shimakawa, Yuichi; Kyoto University, Institute for Chemical Research

ARTICLE

Characterisation of $\text{Pb}_2\text{Rh}_2\text{O}_7$ and $\text{Y}_2\text{Rh}_2\text{O}_7$: An unusual case of pyrochlore stabilisation under high pressure, high temperature synthesis conditions

Received 00th January 20xx,
Accepted 00th January 20xx

DOI: 10.1039/x0xx00000x

Sean D. Injac,^{a,b} Bryce G. Mullens,^c Fabio Denis Romero,^a Maxim Avdeev,^{c,d} Christopher Barnett,^c Alexander K. L. Yuen,^c Midori Amano Patino,^a Supratik Mukherjee,^e Ganapathy Vaitheeswaran,^f David J. Singh,^g Brendan J. Kennedy,^c Yuichi Shimakawa^{*a}

Two novel oxides with compositions $\text{Pb}_2\text{Rh}_2\text{O}_7$ and $\text{Y}_2\text{Rh}_2\text{O}_7$ were synthesised using high pressure, high temperature techniques at 19 GPa and 8 GPa respectively. Structurally, both compounds were determined to crystallise in the cubic pyrochlore structure, space group $Fd\bar{3}m$, with no observed oxygen vacancies. Both oxides have effectively identical Rh-O bond lengths of 1.987 Å and bond-valence sum (BVS) of 4.2 that confirm a Rh^{4+} oxidation state. Physical property measurements for $\text{Pb}_2\text{Rh}_2\text{O}_7$ are consistent with a metallic ground state. This is similar to other $\text{Pb}_2\text{M}_2\text{O}_7$ oxides where $M = \text{Ru}, \text{Ir}, \text{Os}$. $\text{Y}_2\text{Rh}_2\text{O}_7$ represents an unusual case of the lower density (6.356 g/cm^3) pyrochlore structure being stabilised under high pressure conditions, while the analogous, higher density (7.031 g/cm^3) perovskite YRhO_3 is stabilised by synthesis under ambient pressure conditions. The Rh^{4+} state results in a $S = \frac{1}{2}$ magnetic ground state. Magnetisation measurements suggest strong AFM coupling in $\text{Y}_2\text{Rh}_2\text{O}_7$. However, long range AFM order is not observed down to 2 K presumably due to the geometric frustration of the pyrochlore lattice. Specific heat and resistivity measurements indicate a large electronic contribution to the heat capacity. The Wilson ratio of 4.78(11) is well above 2, indicating nearness to magnetism and the likely presence of Rh moments in the background of the conduction electrons. Catalytic activity indicated a greater correlation to other Rh pyrochlores as opposed to dependence upon Rh oxidation state.

Introduction

Pyrochlores oxides are a class of materials that continue to attract interest due to a number of useful phenomena arising from the connectivity and compositional flexibility of the structure.⁽¹⁾ The structure class draws much research interest both in the context of catalytic materials and for electronic and magnetic materials. The compositional flexibility of the pyrochlore structure, which can incorporate oxygen vacancies, can give rise to ionic conductivity and catalytic activity, making the structure class attractive for applications such as solid oxide fuel cells and hydrogen or oxygen evolution catalysis.⁽²⁻⁴⁾ Magnetically, pyrochlores attract interest due to the geometrically frustrated arrangement of cations, giving rise to

exotic magnetic ground states in which properties show a strong dependence upon the nature of oxygen vacancies.⁽⁵⁾

Pyrochlores have the general formula $A_2B_2X_6Y_{1-\gamma}$ in space group $Fd\bar{3}m$, where A is generally a larger cation occupying an eight-fold distorted cubic coordination environment and B is a smaller cation in a six-fold octahedral coordination environment. X and Y are both anions with the X site being fully occupied, forming the corner sharing octahedral network of BX_6 polyhedra and forming six of the eight anion bonds to the A cation. The second anion Y site forms a linear AY_2 coordination environment and has occupancy between $0 \leq \gamma \leq 1$. Disordered vacancies at the Y site maintain the crystal symmetry, in the case of $\gamma = \frac{1}{2}$ the oxygen vacancies can order and the defect pyrochlore structure in space group $F\bar{4}3m$ is observed. Vacancies are also possible at the A -site and in the extreme, materials with large proportions of vacancies such as KO_2O_6 and CsWTaO_6 which have a pyrochlore structure, can form.^(4, 6)

Contrary to the more commonly encountered ABO_3 perovskite structure in which the B cations form a cubic arrangement, the corner sharing octahedral network in pyrochlores gives rise to a tetrahedral arrangements of the A and B cations, which form interpenetrating sublattices. These sublattices can be thought of as forming intersecting Kagome lattices perpendicular to the 111 directions with di-tetrahedral units of cations separating these lattices. One such set of Kagome layers within the B sublattice is represented in Figure 1. This geometrically frustrated arrangement of cations, combined with short range

^a Institute for Chemical Research, Kyoto University, Gokasho, Uji, Kyoto, 611-0011 Japan.

^b Centre for Science at Extreme Conditions and School of Chemistry, University of Edinburgh, Peter Guthrie Tait Road, Edinburgh, EH9 3FD, UK.

^c School of Chemistry, University of Sydney, Sydney, New South Wales 2006, Australia.

^d Australian Nuclear Science and Technology Organisation, Lucas Heights, New South Wales 2234, Australia

^e Advanced Center of Research in High Energy Materials, University of Hyderabad, Prof. C.R. Rao Road, Gachibowli, Hyderabad 500046, Telangana, India

^f School of Physics, University of Hyderabad, Prof. C.R. Rao Road, Gachibowli, Hyderabad 500046 Telangana, India

^g Department of Physics and Astronomy, University of Missouri-Columbia, Columbia, MO65211, USA

antiferromagnetic exchange interactions generally hinders long range magnetic order. Consequently, long range antiferromagnetic order is often observed to be suppressed when either the *A* or *B* sublattices contain magnetic ions. In these cases spin glass, spin ice, or possible spin liquid states are observed.⁽⁷⁾ Ferromagnetic ground states are also reported.^(8, 9)

Pyrochlores materials incorporating platinum group metals (where *B* = Ru, Os, and Ir) have been extensively studied both in the context of physical properties and as oxygen evolution catalysts.^(10, 11) $\text{Bi}_2\text{Ru}_2\text{O}_7$ forms a metallic oxide with disordered oxygen vacancies and is an efficient oxygen electrocatalyst.^(12, 13) The related pyrochlores $\text{Tl}_2\text{Ru}_2\text{O}_7$ and $\text{Cd}_2\text{Ru}_2\text{O}_7$ show temperature-dependent transitions in electronic transport properties that are sensitive to the oxygen stoichiometry, suggesting these *4d* oxides show competing electron localisation and delocalisation effects.^(14, 15) The doping of rare earths at the *A* site of these pyrochlores also tends to result in semiconducting properties that are correlated with the Ru-O-Ru bond angles.⁽¹⁶⁻²⁰⁾ Indeed, $\text{Y}_2\text{Ru}_2\text{O}_7$, with a Ru-O-Ru angle of $128.45(2)^\circ$ is reported to be a semiconductor, whereas a larger angle of 133.1° is observed in the metallic $\text{Bi}_2\text{Ru}_2\text{O}_7$ system.⁽²¹⁾ The similar *5d* containing pyrochlores $\text{A}_2\text{B}_2\text{O}_7$, where *B* = Os, Ir have shown several unusual properties dominated by stronger spin-orbit-coupling (SOC) effects. $\text{Tl}_2\text{Os}_2\text{O}_7$ and $\text{Pb}_2\text{Os}_2\text{O}_7$ show semiconducting and metallic properties, similar to the Ru analogues.⁽²²⁾ $\text{Ln}_2\text{Ir}_2\text{O}_7$ type pyrochlores are of interest due to the presence of long range magnetic ordering, both for the *Ln* cations and for the Ir sublattices that order in all-in-all-out type AFM arrangement.⁽²³⁻²⁵⁾ $\text{Ho}_2\text{Ir}_2\text{O}_7$ and $\text{Dy}_2\text{Ir}_2\text{O}_7$ pyrochlores are also of particular interest due to the fragmenting of magnetic moments.^(26, 27) The relative complexity of magnetic states in the $\text{Ln}_2\text{Ir}_2\text{O}_7$ pyrochlores can be, in part, attributed to the strong spin-orbit coupling of the Ir^{4+} cation and the geometric frustration of the two independent *Ln* and Ir sublattices. Relatively little is known about the Rh pyrochlores. Rh^{4+} is isoelectronic to Ir^{4+} . The *4d* Rh orbitals, compared to the *5d* Ir orbitals, have lower, but still appreciable SOC effects. Moreover, Rh is more flexible in its chemical valence states than Ir, which strongly prefers higher valence, making Rh compounds typically more common for catalytic applications. Moderate SOC effects, coupled with the generally competing electronic

localisation/delocalisation effects of the *4d* transition metals are expected to result in complex electronic and magnetic states for Rh containing oxides.

In addition to their varied electronic and magnetic properties pyrochlores containing platinum group metals have been extensively studied due to their exceptional oxygen evolution properties.^(2, 11, 28) Pyrochlores containing Ru and Ir often show high activity and stability as electrocatalysts. The advantages of the pyrochlore structure type as a catalytic oxide lies with the flexibility of the structure. Here, tuning the structure by the doping of metal elements at the *A* and *B* sites, as well as varying the oxygen occupancy, allows for the activity to be maximised. Notable platinum group metal pyrochlores showing high oxygen evolution reaction (OER) activity are $\text{Y}_2\text{Ru}_2\text{O}_7$ and $\text{Y}_2\text{Ir}_2\text{O}_7$ which show OER activities surpassing RuO_2 and IrO_2 respectively.^(2, 29) The OER activity of Rh pyrochlores is relatively less explored, with $\text{Bi}_2\text{Rh}_2\text{O}_7$ and $\text{Tl}_2\text{Rh}_2\text{O}_7$ having been studied in the context of hybrid Na-air batteries.^(28, 30) Doping of Rh in small quantities as Rh^{4+} into the transition metal pyrochlore $\text{Y}_2\text{Ti}_{2-x}\text{Rh}_x\text{O}_7$ has been found to drastically increase its OER photocatalytic activity, however only a limited doping, of up to 6% Rh could be achieved.⁽³¹⁾ Rh-doped pyrochlores have also attracted attention as catalysts for other reactions, most notably for methane reformation.^(32, 33) The investigation of the physical properties on Rh pyrochlores is generally challenging due to the tendency for rhodium oxides to reduce at the high temperatures required for the synthesis of more complex oxides. As a result Rh, substoichiometry and oxygen deficiency are observed, as well as a tendency towards the lower, diamagnetic Rh^{3+} oxidation state.^(34, 35) High pressure, high temperature (HPHT) synthesis techniques provide a reliable approach to the synthesis of materials incorporating metal cations in higher oxidation states.⁽³⁶⁻³⁸⁾ Using this technique immense oxygen partial pressures can be maintained under high temperatures, generally eliminating oxygen vacancies within the crystal structure, in addition to stabilising higher oxidation states. These materials produced under HPHT conditions are kinetically stable under ambient conditions, and as a result after quenching to room temperature maintain their structural and corresponding chemical and physical characteristics after pressure has been released.

In this paper we have described the preparation of two novel Rh^{4+} pyrochlore oxides and the characterisation of their electronic and magnetic properties. $\text{Pb}_2\text{Rh}_2\text{O}_7$ was found to be a rare example of a mixed valence $\text{Pb}^{2+} / \text{Pb}^{4+}$ transition metal oxide. DFT calculations were undertaken to gain further insight into the experimentally observed properties. These explain the combination of valence states in terms of unusual Pb-O bonding. The activity of these two pyrochlores as catalysts for the oxygen evolution reaction are described and compared to some other Rh oxides.

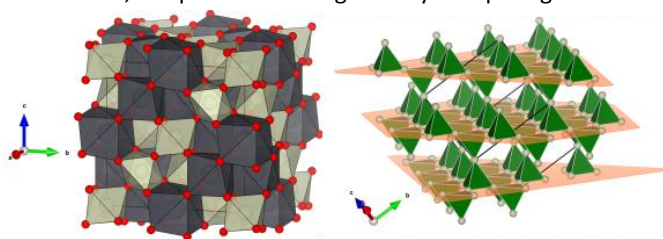


Figure 1: (a) Representation of the $Fd\bar{3}m$ $\text{A}_2\text{Rh}_2\text{O}_7$ pyrochlore crystal structure consisting of alternating tetrahedral arrangements of corner sharing RhO_6 octahedra and eight-fold coordinate AO_8 polyhedra. (b) shows the Rh cation sublattice with the tetrahedral arrangement of cations indicated. The planes indicate one set of 2D Kagome lattices along the 111 direction. The faces of the indicated tetrahedra lie within the Kagome lattices, these lattices are present in all three dimensions with those lying in other orientations omitted for clarity.

Experimental

$\text{Pb}_2\text{Rh}_2\text{O}_7$ and $\text{Y}_2\text{Rh}_2\text{O}_7$ were synthesised using high pressure, high temperature conditions. For $\text{Pb}_2\text{Rh}_2\text{O}_7$, a stoichiometric mixture of PbO_2 and Rh_2O_3 was prepared and sealed into a Pt capsule. The capsule was encased into a pressure transfer medium equipped with a Re heater. Temperature control was achieved through the use of a thermocouple in contact with the end of the Pt capsule. While errors in the reported temperature are negligible, a temperature gradient of approximately 50° is assumed between the ends and centre of the capsule. Reported errors in pressures are given from uncertainties in load vs. pressure calibration curves which tend to increase with increasing pressure. The pressure assembly was compressed using a 6-8 Kawai style multianvil apparatus. The sample was initially pressed to 14(0.4) GPa. The sample was then heated to 1200°C for 1 h before quenching to room temperature, after which the pressure was slowly released and a black powder sample was recovered. Powder X-ray diffraction (XRD) measurements confirmed the formation of a majority pyrochlore phase for this sample with a number of non-indexed peaks indicating incomplete reaction. Significant peak broadening also indicated incomplete phase formation. Further experiments were undertaken at 19(1) GPa and 1200°C heating for 1 h using the same pressure apparatus. Synthesis under these conditions resulted in narrow and well resolved diffraction peaks for the pyrochlore phase, with no impurity peaks evident in laboratory XRD data.

For $\text{Y}_2\text{Rh}_2\text{O}_7$ a stoichiometric mixture of Y_2O_3 , Rh_2O_3 and KClO_4 was ground and sealed into Pt capsules. High pressure, high temperature synthesis was undertaken at 8, 9, 14 and 19 GPa. Syntheses at 14 and 19 GPa were performed using the same pressure apparatus as for $\text{Pb}_2\text{Rh}_2\text{O}_7$. Syntheses at 8(0.2) and 9(0.2) GPa were carried out using a cubic anvil DIA pressure apparatus incorporating graphite heaters. All samples were heated to 1200°C for 1 h before quenching to room temperature. Final samples were a black powder.

Phase purity was examined for all synthesised samples by analysing their laboratory powder X-ray diffraction (XRD) patterns. XRD patterns were measured using a Bruker D8 powder diffractometer equipped with a Cu-K α radiation source. Thermogravimetric analysis (TGA) data was collected between room temperature and 800°C using a 95% Ar, 5% H_2 flow gas. Synchrotron powder diffraction (SXRD) measurements were undertaken on at the BL02B2 beamline at SPring-8, Japan. Powder samples were housed in 0.2 mm diameter quartz capillaries which were rotated perpendicular to the incident X-ray beam. Data were collected at room temperature using wavelengths of 0.774488 \AA and 0.495819 \AA for $\text{Pb}_2\text{Rh}_2\text{O}_7$ and $\text{Y}_2\text{Rh}_2\text{O}_7$ respectively. Neutron powder diffraction data were collected using the high-resolution diffractometer ECHIDNA at the Australian Centre for Neutron Scattering (ACNS), operated by the Australian Nuclear Science and Technology Organisation (ANSTO), Australia.⁽³⁹⁾ Data were collected using powder samples produced from multiple synthesis runs that were performed under the same experimental conditions. Datasets were collected at room temperature using incident neutrons of

wavelength 1.6215 \AA for both samples. An additional dataset using neutrons of wavelength 1.300 \AA was collected for $\text{Pb}_2\text{Rh}_2\text{O}_7$ to probe for displacement of the Pb cations. Rietveld refinement was carried out against diffraction data using the FullProf analysis suite.

X-ray photoelectron spectroscopy (XPS) data were measured using a Thermo Fisher K-Alpha+ instrument. The X-ray source was a monochromated Al K α beam of 1486.6 eV with the beam width set to $400\text{ }\mu\text{m}$. The electron flux and energy of the emitted photoelectrons were measured using a 180° double-focusing hemispherical analyser, with a 128-channel detector scanning between 10-1350 eV. The powder samples were fixed to an aluminum sample stage using carbon tape. Survey spectra were measured with an analyser pass energy of 200 eV, and 10 scans were measured with a dwell time of 10 ms. Higher resolution spectra of the elements of interest were collected with a pass energy of 50 eV. Again, 10 scans per spectra were collected with a dwell time of 50 ms.

Bulk magnetisation measurements were carried out using a Quantum Design PPMS for $\text{Pb}_2\text{Rh}_2\text{O}_7$ and a Quantum Design MPMS-XL system for $\text{Y}_2\text{Rh}_2\text{O}_7$. Data were collected under zero field cooled (ZFC) and field cooled (FC) conditions, the ZFC data were collected on heating while FC data was collected on heating and cooling. Isothermal magnetisation measurements were undertaken at 5 K and 300 K, collected to $\pm 50\text{ kOe}$. Variable temperature heat capacity and resistivity measurements were carried out on pellets yielded directly from the high pressure, high temperature synthesis to maximise sample density. These measurements were carried out on a Quantum Design PPMS system between 2 K and 300 K. Heat capacity data were collected using the 2-tau relaxation technique, resistivity measurements were collected in a 4-probe arrangement using silver electrodes and in AC drive mode.

For electrocatalysis, inks were prepared by adding finely ground metal oxide (10 mg) to a solution of milli-Q water ($475\text{ }\mu\text{L}$), isopropanol (RCI Labscan HPLC grade; $125\text{ }\mu\text{L}$), and 5 wt% Nafion (Aldrich; $10\text{ }\mu\text{L}$). The mixture was then sonicated for 10 min. Glassy carbon (GC) electrodes (5 mm diameter, supplied by BAS) were cleaned, then polished on a polishing pad with an aqueous slurry of $0.3\text{ }\mu\text{m}$ alumina, rinsed with milli-Q water, then ethanol, and dried under nitrogen to leave a clean and shiny surface. Inks were agitated on a vortex mixer, then a $10\text{ }\mu\text{L}$ aliquot was drop-cast onto the cleaned GC electrode. The drops were allowed to air-dry in a fumehood, resulting in an even coating, then dried at 60°C in an oven for 15 min. The catalyst loading on the GC electrodes was 0.836 mg/cm^2 .

Linear sweep voltammograms were collected using the following setup: Ag/AgCl reference electrode (BAS); platinum wire as a counter electrode; the drop-cast ink as working electrode; and 1 M aqueous NaOH as the electrolyte. Linear sweeps were collected at 5 mV/s with a rotation of 1500 rpm. Electrochemical surface area measurements were obtained by sweeping 200–100 mV (vs Ag/AgCl) after a 10 s rest period, at scan rates of 5, 10, 25, 50, 100, 200, 400, 800 mV/s. The slope of the non-faradaic current vs sweep rate was divided by 0.040 mF/cm^2 to obtain the surface area.

The density functional theory (DFT) calculations were performed using the Vienna Ab initio Simulation Package (VASP) code (version 5.4.4), based on projector augmented wave (PAW) formalism.(40-42) The generalised gradient approximation (GGA) with the functional of Perdew, Burke and Ernzerhof (PBE) was used.(43) The maximum plane wave energy cut-off was set to 600 eV, which is a highly converged value for these PAW pseudopotentials. An $8 \times 8 \times 8$ Monkhorst-Pack k-point mesh was used for integrating the Brillouin zone during self-consistency.(44) The Y ($4d^1 5s^2$), Pb ($5d^{10} 6p^2$), Rh ($4d^8 5s^1$) and O ($2p^4 2s^2$) electrons were included as valence states. In obtaining the ground state configurations the energy and force convergence criteria were set to 10^{-6} eV and 10^{-2} eV/atom respectively. Considering the presence of local moments indicated by experiment, the GGA+U method was used which is well suited to such cases.(45) It is noted that hybrid functional calculations for example with the HSE06 can yield parameter free predictions of band gaps of insulating oxides often more reliably than DFT+U calculations, which require a parameter.(46, 47) However, such calculations can introduce errors in metallic materials especially in proximity to magnetism, and therefore are not used here.(48, 49) For Rh a Hubbard U value of 4 eV was implemented. SOC were also considered using the fully relativistic PAW potentials. Results for $\text{Pb}_2\text{Rh}_2\text{O}_7$ were cross-checked using the general potential linearised augmented planewave method as implemented in the WIEN2k code.(50)

Results and Discussion

The structures of $\text{Pb}_2\text{Rh}_2\text{O}_7$ and $\text{Y}_2\text{Rh}_2\text{O}_7$:

Laboratory X-ray diffraction data collected from $\text{Pb}_2\text{Rh}_2\text{O}_7$ could be indexed on the basis of a cubic cell with lattice parameters 10.105 Å, consistent with the formation of a material adopting the pyrochlore structure. Laboratory XRD patterns collected for $\text{Y}_2\text{Rh}_2\text{O}_7$ samples synthesized at 1200 °C and pressures of 8 or 9 GPa confirmed the formation of a pyrochlore phase but also revealed the presence of a secondary perovskite YRhO_3 phase. Increasing the pressure of the reaction to 14 or 19 GPa yielded samples that contained a mixture of YRhO_3 perovskite and the high pressure form of RhO_2 .(51) It is noted that synthesis at ambient pressure is reported to stabilise the YRhO_3 perovskite phase.(52) The perovskite phase was present in varying amounts in all samples of $\text{Y}_2\text{Rh}_2\text{O}_7$. The sample synthesised at 8 GPa contained the lowest mass fraction of YRhO_3 perovskite and was thus used for all further measurements. TGA data collected for $\text{Pb}_2\text{Rh}_2\text{O}_7$ and $\text{Y}_2\text{Rh}_2\text{O}_7$ were consistent with full oxygen stoichiometry. Samples were heated in a reducing atmosphere to 800 °C, where under these conditions $\text{Y}_2\text{Rh}_2\text{O}_7$ was reduced to a mixture of Y_2O_3 and Rh metal while $\text{Pb}_2\text{Rh}_2\text{O}_7$ was reduced to the base metals as confirmed by laboratory XRD (details in SI). Rietveld refinements were carried out against SXR and NPD data collected at room temperature. The results are shown in Figure 2 and the refined parameters are tabulated in Table 1. Refinements for both $\text{Pb}_2\text{Rh}_2\text{O}_7$ and for $\text{Y}_2\text{Rh}_2\text{O}_7$ were consistent with a pyrochlore structure in space group $Fd\bar{3}m$. No peaks indicative of the related $F\bar{4}3m$ defect pyrochlore

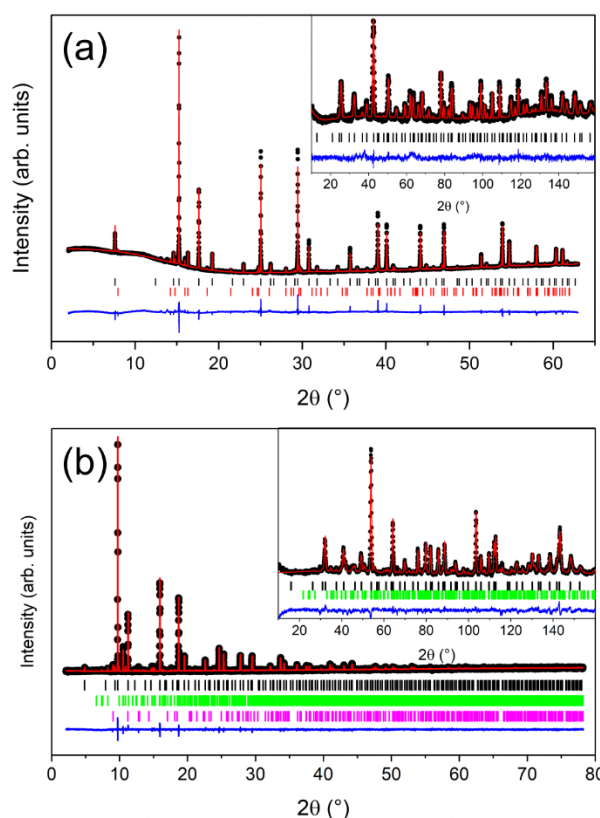


Figure 2: Rietveld refinement profiles for $\text{Pb}_2\text{Rh}_2\text{O}_7$ and $\text{Y}_2\text{Rh}_2\text{O}_7$, are shown in (a) and (b) respectively (wRp = 2.39 and 2.35). Data is indicated by black dots, the calculated profile is indicated in red and blue shows the difference plot. The main plot shows the refinement profile for SXR data, black tick marks indicate the peak positions for the main pyrochlore phase, red tick marks indicate those for the PbRhO_3 impurity, green ticks show the YRhO_3 impurity ($f_w = 10.1(3)\%$) and magenta indicates the RhO_2 impurity ($f_w = 1.8(2)\%$). The inserts show refinement profiles carried out against NPD data collected using neutrons of 1.30 and 1.62 Å for $\text{Pb}_2\text{Rh}_2\text{O}_7$ and $\text{Y}_2\text{Rh}_2\text{O}_7$, respectively (wRp = 3.78 and 4.07).

structure, which would correspond to $\text{Pb}_2\text{Rh}_2\text{O}_{6.5}$ and $\text{Y}_2\text{Rh}_2\text{O}_{6.5}$, and are observed for both $\text{Pb}_2\text{Ru}_2\text{O}_{6.5}$ and $\text{Pb}_2\text{Ir}_2\text{O}_{6.5}$ were observed.(53-55) This is indicative of full occupancy of the oxygen 8b site for both compounds. The final refinements were carried out against combined SXR and NPD datasets, in these refinements the absorption parameter of SXR data was treated as a variable. As a result the reported B_{iso} values in Table 1 arise from fits to the NPD datasets. Varying oxygen occupancy at the 8b or O2 site, taken to lie within the channels of the pyrochlore consistently resulted in full occupancy, consistent with the results from the TGA. The YRhO_3 perovskite impurity was fitted using a model in space group $Pbnm$. Crystallographic data for this compound are given in the SI in table SI1. Refinement plots for $\text{Pb}_2\text{Rh}_2\text{O}_7$ and $\text{Y}_2\text{Rh}_2\text{O}_7$ are given in Figure 2a and 2b respectively. Refined parameters are tabulated in Table 1, we further calculated the optimised lattice parameters at 0 GPa for the compounds in order to confirm the accuracy of DFT calculations. The optimized lattice parameters are $a = 10.201$ Å and $a = 10.149$ Å for $\text{Pb}_2\text{Rh}_2\text{O}_7$ and $\text{Y}_2\text{Rh}_2\text{O}_7$ respectively, compared with the experimental lattice parameters of 10.10568 Å and 10.11834 Å respectively. Details of the optimised structures are given in SI Table SI2. From these calculations the bulk modulus of both compounds was derived

from the energy vs. volume curves by fitting a 4th-order Birch-Murnaghan equation of state.(56) The computed bulk modulus values for $\text{Pb}_2\text{Rh}_2\text{O}_7$ and $\text{Y}_2\text{Rh}_2\text{O}_7$ are 173.50 GPa and 191.31 GPa, respectively. When compared with the bulk modulus values for other pyrochlores like $\text{Tb}_2\text{Ti}_2\text{O}_7$ (168 GPa), and $\text{Yb}_2\text{Hf}_2\text{O}_7$ (220 GPa), these values align closely.(57, 58) Such similarities suggest the inherent hardness characteristics exhibited by these pyrochlore materials.

The Rietveld refinements for the sample of $\text{Y}_2\text{Rh}_2\text{O}_7$ synthesised at 8 GPa indicated a 10.1(1) wt % YRhO_3 impurity in both the SXR and NPD data and a small (1.8(2) wt %) RhO_2 impurity in the SXR data. The latter was not detected in the NPD data. The denser perovskite phase YRhO_3 has been reported previously from standard solid-state synthesis under ambient pressure. The phase was reported to exhibit an orthorhombically distorted perovskite structure in space group $Pnma$.(59) In our study, this phase formed the majority of the synthesised product when the reaction was undertaken at 14 GPa together with a RhO_2 minor phase; no pyrochlore phase was detected in this sample. Synthesis at 19 GPa also resulted in the formation of the perovskite phase with a RhO_2 secondary phase. These results suggest that the Rh^{3+} perovskite phase is the thermodynamically preferred product over the entire pressure range and that the metastable pyrochlore phase is synthesised over a narrow pressure window that is optimal for the stabilisation of Rh^{4+} , but not sufficiently high to yield the high-density perovskite phase. In general, higher pressures favour the formation of the higher density product. Indeed, in several cases a perovskite phase can be obtained from the associated pyrochlore composition when synthesis is undertaken under HPHT conditions.(60, 61) The theoretical densities of the $\text{Y}_2\text{Rh}_2\text{O}_7$ pyrochlore and YRhO_3 perovskite phase, derived from Rietveld fits to SXR data, are 6.356 and 7.031 g/cm^3 respectively. The density of the perovskite phase recovered from synthesis at 8 GPa is in good agreement with the density derived from published crystallographic data for samples synthesised at ambient pressure of 7.045 g/cm^3 .(59) The large difference in densities of the pyrochlore $\text{Y}_2\text{Rh}_2\text{O}_7$ and perovskite YRhO_3 suggests that the pyrochlore $\text{Y}_2\text{Rh}_2\text{O}_7$ may potentially be synthesised at ambient pressure under oxidising conditions sufficient to stabilise Rh^{4+} .

Table 1: Crystallographic structure parameters derived from Rietveld refinements for $\text{Pb}_2\text{Rh}_2\text{O}_7$ and $\text{Y}_2\text{Rh}_2\text{O}_7$.

Composition	$\text{Pb}_2\text{Rh}_2\text{O}_7$	$\text{Y}_2\text{Rh}_2\text{O}_7$
Space group	$Fd\bar{3}m$	$Fd\bar{3}m$
a (Å)	10.10568(2)	10.11834(5)
Volume (Å ³)	1032.146(4)	1035.924(9)
$A(x,y,z)$ 16c	$\frac{1}{2}, \frac{1}{2}, \frac{1}{2}$	$\frac{1}{2}, \frac{1}{2}, \frac{1}{2}$
$\text{Rh}(x,y,z)$ 16d	0, 0, 0	0, 0, 0
$\text{O1}(x,y,z)$ 48f	0.33607(15), 1/8, 1/8	0.33536(17), 1/8, 1/8
$\text{O2}(x,y,z)$ 8b	3/8, 3/8, 3/8	3/8, 3/8, 3/8
$A B_{\text{iso}}$ (Å ²)	0.350(34)	0.152(39)
$\text{Rh} B_{\text{iso}}$ (Å ²)	0.012(39)	0.070(34)
$\text{O1} B_{\text{iso}}$ (Å ²)	0.265(29)	0.293(33)

$\text{O2} B_{\text{iso}}$ (Å ²)	0.19(7)	0.044(94)
$A-\text{O1}$ (Å)	2.4347(11)	2.4443(12)
$A-\text{O2}$ (Å)	2.1879	2.1907
$\text{Rh}-\text{O1}$ (Å)	1.9880(10)	1.9863(11)
$\text{Rh}-\text{O1}-\text{Rh}$ (°)	127.8(3)	128.46(3)
A BVS	3.42	3.16
Rh BVS	4.19	4.20
wRp SXR	2.39	2.35
wRp NPD (1.622 Å)	4.42	4.07
wRp NPD (1.300 Å)	3.78	

Rietveld analysis of SXR data for $\text{Pb}_2\text{Rh}_2\text{O}_7$ revealed the presence of a small number of unfitted peaks that could not be matched to any PbO_x or RhO_x oxides available in the Inorganic Crystal Structure Database (ICSD). Attempts to index these peaks were consistent with a hexagonal unit cell with cell lengths of $a = b = 3.6116$ and $c = 11.1531$ Å. The a and b cell lengths are too short to stabilise a hexagonal or cubic perovskite structure, rather a value of ~ 4 Å is expected for a cubic perovskite.(62) These lattice constants are similar to those reported for the high temperature form of YMnO_3 .(63) A structural model for PbRhO_3 was developed in space group $P6_3/mmc$ and inclusion of this in the refinements against the SXR data accounted for all previously unfitted peaks. The calculated weight fraction of hexagonal PbRhO_3 was 6.32(18) wt%. The refined crystallographic parameters for this phase are given in the Supplementary Information. The inherent inaccuracy in determining the oxygen positional parameters for a minor phase, even from SXR data, makes assignment of the Rh oxidation state in this compound difficult. Nevertheless, the trigonal bipyramidal coordination environment of the Rh cation would result in a magnetic ground state for both Rh^{3+} and Rh^{4+} , being $S = 2$ and $S = 5/2$ respectively, thus this phase will contribute to the bulk magnetisation measurements described below.

The Rh–O bond distances in $\text{Pb}_2\text{Rh}_2\text{O}_7$ and $\text{Y}_2\text{Rh}_2\text{O}_7$ are, within experimental uncertainty, identical at 1.98 Å, which is comparable to that seen in other Rh^{4+} oxides such as RhO_2 (1.99 Å) and $\text{Sr}_3\text{Rh}_2\text{O}_7$ (1.987 Å) and is significantly shorter than seen in Rh^{3+} oxides such as 2.03 Å in CuRh_2O_4 .(64, 65) The calculated bond valence sums of 4.19 and 4.20, respectively, are consistent with Rh^{4+} for both compounds. This is somewhat surprising in the case of $\text{Pb}_2\text{Rh}_2\text{O}_7$, since it would imply a nominal Pb valence of Pb^{3+} , which is very unusual. The slightly higher BVS of 4.2 compared to the expected valence of 4 may indicate slight over-bonding of the Rh cation, which is typical of oxides synthesised at high pressures. The BVS for the Y cation in $\text{Y}_2\text{Rh}_2\text{O}_7$ is 3.16, supporting the crystal structure determination and further verifying the presence of a Rh^{4+} oxidation state and full oxygen stoichiometry.

The BVS of the Pb cation $\text{Pb}_2\text{Rh}_2\text{O}_7$ is 3.42 which is intermediate between Pb^{2+} and Pb^{4+} suggesting an average oxidation state of Pb^{3+} on the A-site. Since trivalent Pb is unknown this suggests there is a mixture of Pb^{2+} and Pb^{4+} on the A-site. As described in more detail below, DFT calculations using WIEN2k in which the atomic coordinates were fully relaxed yield similarly high bond

valence sums for Pb, specifically 2.96. Sleight has previously described the synthesis of $\text{Pb}_2\text{Rh}_2\text{O}_7$ at 0.3 GPa and 700°C and proposed that the observed unit cell parameter of $a = 10.112(2)$ Å is inconsistent with a mixed $\text{Pb}^{2+}/\text{Pb}^{4+}$ arrangement that would have $a = 10.3$ Å.(66) Sleight consequently concluded that the system was $(\text{Pb}^{4+})_2(\text{Rh}^{3+})_2\text{O}_7$. The unit cell parameter obtained in the present work is comparable to that reported by Sleight 10.10568(2) vs 10.112(2) Å indicating that the two samples most likely have the same cation distribution. In his early study Sleight did not refine the structure and hence did not determine the Rh–O or Pb–O distances. The Rh–O bond distances observed here demonstrate that the Rh is present as Rh^{4+} , which is consistent with Pb having an average oxidation state of Pb^{3+} . The Rietveld refinements provide no evidence for ordering of the Pb^{2+} and Pb^{4+} cations indicating a random distribution of these over the eight coordinate A site. This is rationalised by charge order being frustrated in a triangular lattice analogous to magnetic frustration as observed in the pyrochlore $\text{Pb}_2\text{FeTeO}_{6.5}$.(61) Alternately, it may be that the Pb disproportionation is ordered, but with a very complex order due to the pyrochlore lattice that is not detected. Weller and co-workers concluded that the analogous Os compound contained a mixed lead oxidation states on the A-site and that Os^{4+} exclusively occupies the octahedral sites.(22)

To further probe the valence states of the cations XPS data were measured for both samples. For the $\text{Y}_2\text{Rh}_2\text{O}_7$ sample the Rh 3d line has a binding energy of approximately 310 eV that overlaps with the Y 3p_{1/2} line. The Y 3d spectrum was not a simple spin-orbit double but rather contained at least two species. Further, the C1s signal from the $\text{Y}_2\text{Rh}_2\text{O}_7$ sample contained a strong peak near 286 eV suggesting that the surface of the sample contained appreciable amounts of absorbed carbonate after storage for several months. The Pb 4f spectra for $\text{Pb}_2\text{Rh}_2\text{O}_7$ displayed in Figure 3a shows a distinct splitting of both the 4f_{7/2} and 4f_{5/2} lines, indicating the presence of multiple oxidation states. These features were fitted with two peaks constrained to be equal in full width at half maximum (FWHM) and area to reflect the equal Pb^{2+} : Pb^{4+} content. The position and energy difference between these peaks is in good agreement with previous literature, with the peak of Pb^{2+} at higher binding energy than Pb^{4+} due to the screening response of the mobile conduction electrons.(67, 68) A third set of peaks was also added to assist in the fitting of the residual intensity. This peak, at higher binding energy, has been observed in $\beta\text{-PbO}_2$ and is the result of the plasmon structure.(69) The Rh(3d) spectra (Figure 3b) is

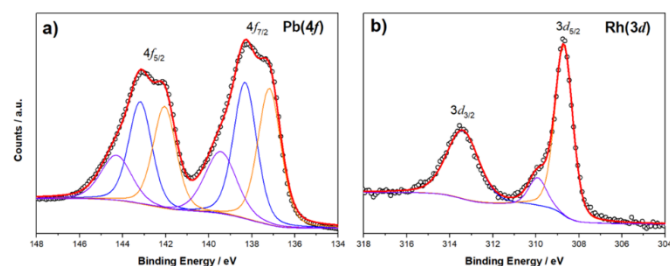


Figure 3: The X-ray photoelectron spectroscopy (XPS) of $\text{Pb}_2\text{Rh}_2\text{O}_7$ showing (a) the Pb 4f line and (b) the Rh 3d line.

also in good agreement with literature, with a single 3d_{5/2} line and a significantly broadened 3d_{3/2} line due to the Coster-Kronig effect.(70, 71) All spectra have been energy corrected, and reported in Table 2.

The crystallographic and XPS study unequivocally demonstrates that we have formed $(\text{Pb}^{2+}\text{Pb}^{4+})\text{Rh}^{4+}_2\text{O}_7$. It is likely that the higher than expected BVS for the Pb is due to the very short Pb–O2 distances, where O2 lies within the centre of four Pb cations in a tetrahedral arrangement as indicated in Figure 1. This compression of the Pb sublattice is likely stabilised by the rigid RhO_6 octahedral framework, reflecting the metastable nature of oxides synthesised under extreme pressures.

Table 2: Reported Pb 4f and Rh 3d binding energies for $\text{Pb}_2\text{Rh}_2\text{O}_7$

	Assignment	Experimental (eV)	Literature (eV)	
Pb 4f _{7/2}	Pb ²⁺	138.4	138.1 (PbO) ¹	138.6 (Pb ₃ O ₄) ¹
	Pb ⁴⁺	137.3	137.2 (PbO ₂) ¹	137.6 (Pb ₃ O ₄) ¹
Rh 3d _{5/2}	Rh ⁴⁺	308.7	308.6 (RhO ₂) ⁵	

Catalytic activity of Rh⁴⁺ compounds:

The catalytic activity of the Rh containing pyrochlores were probed by comparing their performance as catalysts for the oxygen evolution reaction (OER) under alkaline conditions with that of some other rhodium oxides; namely RhNbO_4 , $\text{Bi}_2\text{Rh}_2\text{O}_7$, δ , and Rh_2O_3 . The conditions for the measurements were those recommended in the literature.(72) Linear sweep voltammograms were collected for inks prepared with each of the catalysts. Each ink was drop-cast onto a 5 mm Glassy Carbon

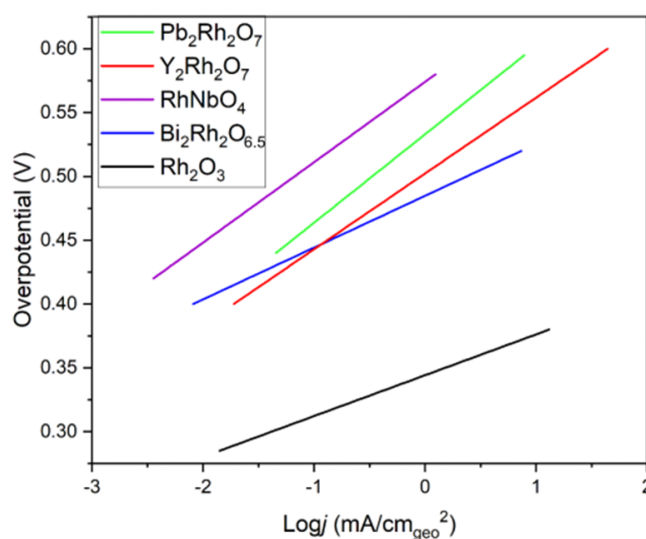


Figure 4: Comparison of Tafel plots of crystalline pyrochlores under alkaline conditions (0.100 M NaOH). Solid lines are the average of duplicate runs and indicate the linear region of the Tafel curves obtained. In all cases the catalyst loading was 0.836 mg cm⁻²; Rotation 1500 rpm; CE: Pt(s); overpotential corrected to the reversible hydrogen electrode.

Rotating Disc Electrode (GC-RDE). The RDEs were rotated at 1500 rpm to remove diffusion as a variable in the analysis. Tafel plots for the oxides are shown in Figure 4 and the results tabulated in Table 3 summarise the overpotential (η) and OER activities. Only Rh_2O_3 was able to achieve 10 mA/cm^2 charge density with an overpotential $\leq 0.45 \text{ V}$, having $\eta = 0.376 \text{ V}$. The Tafel plots for $\text{Pb}_2\text{Rh}_2\text{O}_7$ and $\text{Y}_2\text{Rh}_2\text{O}_7$ have similar slopes, indicating similar kinetics, although $\text{Y}_2\text{Rh}_2\text{O}_7$ required a slightly lower overpotential indicating a lower thermodynamic barrier to OER. The slopes of these two pyrochlores are comparable to that observed for the Rh^{3+} oxide RhNbO_4 . The catalytic activity of the Rh^{3+} pyrochlore oxide $\text{Bi}_2\text{Rh}_2\text{O}_7$ was also investigated, and this had a shallower slope than the two Rh^{4+} pyrochlores, and was comparable to the slope for Rh_2O_3 . Overall, these data suggest slightly poorer kinetics for Rh^{4+} , however the three pyrochlore curves have comparable overpotentials, suggesting the mechanism of OER is more closely correlated to structure rather than Rh oxidation state and that the presence of other cations acts as a thermodynamic barrier to OER compared to the binary oxide.

Table 3: Comparison of the electrochemical results for $\text{Pb}_2\text{Rh}_2\text{O}_7$ and $\text{Y}_2\text{Rh}_2\text{O}_7$ with other rhodium oxides.

Pyrochlore	Slope (V/dec)	Overpotential at $\text{Log}j=0$ (V)	η_{10} (V)
Rh_2O_3	0.032(2)	0.344(7)	0.376
$\text{Bi}_2\text{Rh}_2\text{O}_7$	0.041(1)	0.485(8)	0.525
$\text{Y}_2\text{Rh}_2\text{O}_7$	0.059(7)	0.502(5)	0.562
$\text{Pb}_2\text{Rh}_2\text{O}_7$	0.069(3)	0.532(14)	0.601
RhNbO_4	0.063(2)	0.574(17)	0.637

Magnetic and electronic properties:

Magnetic susceptibility measurements for both $\text{Y}_2\text{Rh}_2\text{O}_7$ and $\text{Pb}_2\text{Rh}_2\text{O}_7$ are shown in Figure 5, and isothermal magnetisation

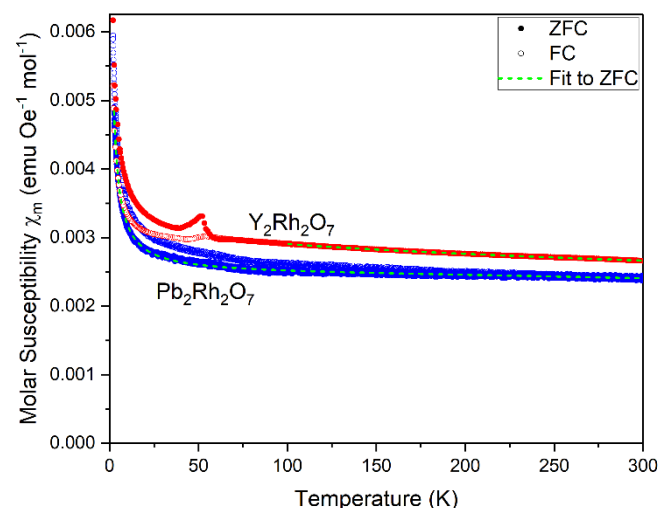


Figure 5: Temperature dependent magnetisation data for $\text{Pb}_2\text{Rh}_2\text{O}_7$ and $\text{Y}_2\text{Rh}_2\text{O}_7$ is shown as blue and red markers respectively. Data collected under ZFC and FC conditions are plotted with closed and open circles respectively. The fits to ZFC data are indicated by dashed green lines.

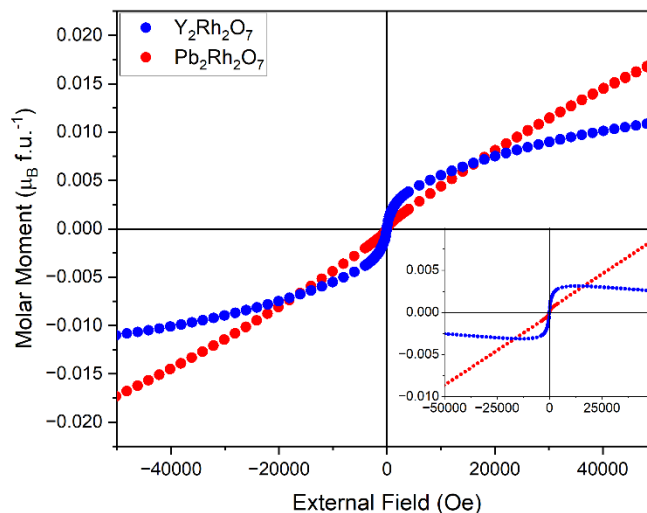


Figure 6: Isothermal magnetisation data collected for $\text{Pb}_2\text{Rh}_2\text{O}_7$ and $\text{Y}_2\text{Rh}_2\text{O}_7$. The main plot indicates data collected at 5 K and the insert shows data collected at 300 K.

measurements collected at 2 K and 300 K are shown in Figure 6. Fits to the paramagnetic region of temperature dependent magnetisation data (taken to be $T > 75 \text{ K}$ for $\text{Y}_2\text{Rh}_2\text{O}_7$, and the entire temperature region for $\text{Pb}_2\text{Rh}_2\text{O}_7$) are also indicated. The paramagnetic region of the ZFC data was fit using the expression $\chi = \frac{C}{T - \Theta_w} + \chi_0$ which models temperature independent and Curie-Weiss contributions to the magnetisation data. The parameters derived from these fits are given in Table 4. Fits to the paramagnetic region were consistent with a predominately temperature independent magnetic ground state for $\text{Pb}_2\text{Rh}_2\text{O}_7$, with a negligible Curie-Weiss (CW) type contribution as indicated by a very low $\mu_{\text{eff}} = 0.17 \mu_B$ per Rh. This is significantly below the expected value of $1.73 \mu_B$ for the $S = \frac{1}{2} \text{ Rh}^{4+}$ cation. The effectively zero value of Θ_w indicates no appreciable magnetic coupling between the Rh cations. The isothermal magnetisation curve collected at 5 K further demonstrates weak paramagnetism, although the curve collected at 300 K reveals an anomaly that is believed to be due to the presence of a small amount of a magnetic impurity in the sample. It is unknown if this behaviour is caused by the secondary PbRhO_3 phase or if it is due to sample contamination. At both temperatures, no hysteresis is observed which discounts a ferromagnetic contribution. Overall, these magnetic measurements suggest itinerant electrons for $\text{Pb}_2\text{Rh}_2\text{O}_7$, resulting in a Pauli paramagnetic ground state. This observation is similar to that found in the related Pb-containing pyrochlores Pb_2M_2O_7 with $M = \text{Ru}, \text{Ir}, \text{Os}, \text{ and } \text{Re}$.(73)

Table 4: Magnetic and physical parameters for $\text{Pb}_2\text{Rh}_2\text{O}_7$ and $\text{Y}_2\text{Rh}_2\text{O}_7$ derived from fits to temperature dependent magnetisation and heat capacity data.

Composition	$\text{Pb}_2\text{Rh}_2\text{O}_7$	$\text{Y}_2\text{Rh}_2\text{O}_7$
C (emu K mol^{-1})	$8.02(3) \times 10^{-3}$	$8.96(7) \times 10^{-2}$
Θ_w (K)	$-0.81(2) \text{ K}$	$-123(10) \text{ K}$
μ_{eff} (μ_B)	0.25	0.85
χ_0 (emu mol^{-1})	$2.45(1) \times 10^{-3}$	$2.51(1) \times 10^{-3}$
γ ($\text{J K}^{-2} \text{ mol}^{-1}$)		$3.43(15) \times 10^{-2}$

β (J K ⁻⁴ mol ⁻¹)		2.31(5) × 10 ⁻⁴
Θ_{debye} (K)		452(1)
R_w		4.78(11)

Temperature-dependent magnetisation measurements for Y₂Rh₂O₇ show a feature at approximately 52 K. This feature is most likely not associated with a magnetic transition of the main phase due to suppression of the anomaly under field-cooled measurement conditions. It is noted that the two detected impurities, YRhO₃ and RhO₂ are diamagnetic and paramagnetic respectively and thus cannot give rise to the observed feature. Fits to the paramagnetic region above 75 K show predominately temperature-independent behaviour. The CW contribution is greater than that derived for Pb₂Rh₂O₇, however the calculated μ_{eff} of 0.60 μ_B is still significantly lower than that indicated by the spin only value of 1.73 μ_B . While it is noted that SOC will play a role in reducing the magnetic moments of the 4d and 5d transition metals, this effect is unlikely to result in such a large reduction when compared to similar Rh- and Ru-containing oxides.(74, 75) Fits to the paramagnetic region also indicated a large, negative Weiss constant of -123(10) K, which is consistent with weak AFM coupling of Rh magnetic moments. Stronger AFM coupling is observed in the related Y₂Ru₂O₇, which is a spin-glass with a freezing temperature of approximately 80 K.(76) Overall, these results suggest weak antiferromagnetic coupling with a comparable temperature-independent paramagnetic

that show AFM coupling this magnetic frustration suppresses long range antiferromagnetic order.(76, 77) However, the absence of a displaced magnetisation curve in the isothermal magnetisation measurements at 5 K for Y₂Rh₂O₇ as well as comparable ZFC and FC curves below 50 K indicate that Y₂Rh₂O₇ is not a spin glass.

Analysis of the low temperature heat capacity data for Pb₂Rh₂O₇ shows a distinct trend towards zero heat capacity at low temperature. The relationship between C/T and T² is clearly nonlinear in the region of 0 < T² < 100 K², as a result no fits to a linear equation of the form C/T = $\beta T^2 + \gamma$ were attempted. Conversely Y₂Rh₂O₇ shows excess heat capacity as the temperature approaches 0 K. While this excess heat capacity could be consistent with a spin ice state, a spin ice state would be inconsistent with the magnetisation measurements and the absence of a feature in heat capacity data. The C/T vs T² plot for Y₂Rh₂O₇ was fitted to the linear equation described above, and the resulting electronic and lattice contributions to heat capacity (γ and β respectively) are given Table 4. The large electronic contribution (Sommerfield constant) of $\gamma = 34.3(15)$ mJ K⁻² mol⁻¹, results in a calculated Wilson ratio ($R_w = \frac{4}{3} \left(\frac{\pi k_B}{g \mu_B} \right)^2 \frac{\chi_0}{\gamma}$ with g = 2) of $R_w = 4.78$. This value is significantly higher than that expected for a standard metallic Fermi gas ($R_w = 1$), and is also inconsistent with a simple Fermi liquid with electron correlations, which typically would lead to $R_w < 2$. Rather, it suggests a degree of electron localisation with correlated local moments embedded in the conduction

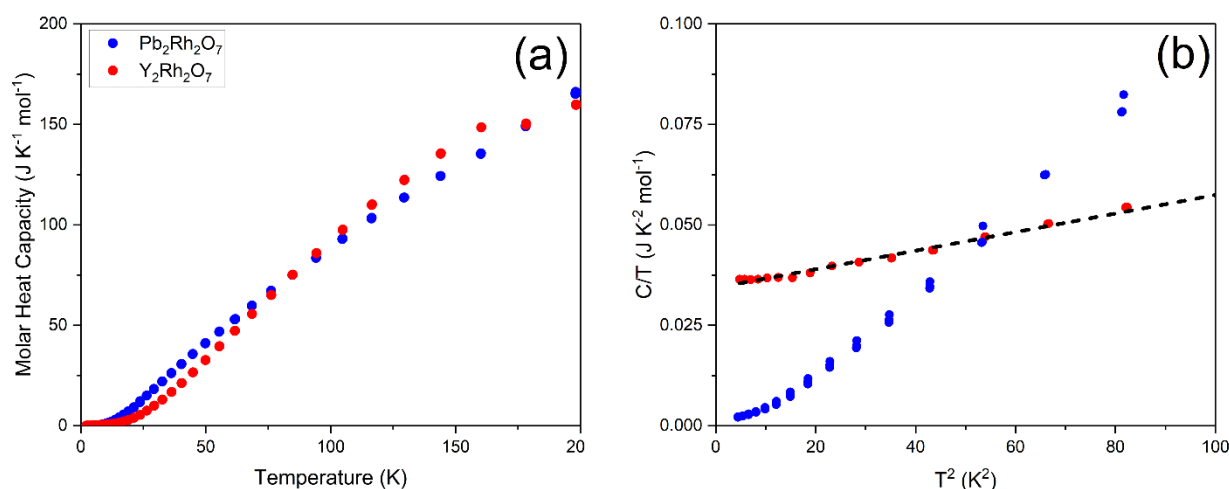


Figure 7: Temperature dependent heat capacity data is shown plotted in (a), no features consistent with structural or magnetic transitions are observed. A plot of C/T vs. T² is shown in (b), a linear fit to the data for Y₂Rh₂O₇ is indicated with a dashed line

contribution to Pb₂Rh₂O₇. Remarkably, although from a structural point of view the Rh environment and inferred valence are similar in the two compounds, the Pb compound does not show localised Rh moments.

The temperature-dependent heat capacity measurements, given in Figure 7, do not show any lambda type features down to 2 K for either compound. This confirms the absence of magnetic order for Y₂Rh₂O₇. This result is expected considering the geometrically frustrated tetrahedral arrangement of cations in the pyrochlore structure. In the vast majority of pyrochlores

electrons, consistent with the observed AFM coupling and Pauli paramagnetism. It should be noted that the presence of a paramagnetic impurity such as RhO₂ will result in an increase in the Wilson ratio, due to an increase in χ_0 determined from fits to the magnetisation data. Since the SXR D measurements indicate the impurity is present at about 1 wt% and is unlikely to significantly affect the determined χ_0 , or the subsequently calculated R_w values. It is unknown what impact the YRhO₃ impurity has on the determined Sommerfield constant, as the authors were not able to locate a reported heat capacity

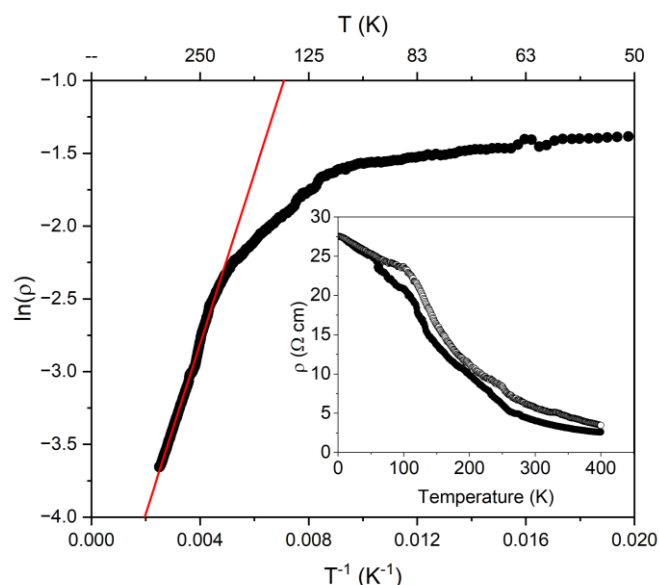


Figure 8: Arrhenius plot of resistivity data $\ln(\rho)$ vs T^{-1} is shown in the main figure, a linear relationship between 400 K and 250 K is indicated by a red line, which does not persist to low temperature. The inset shows temperature dependent resistivity data collected between 2 K and 400 K. Closed circles indicate data collected on cooling and open circles indicate data collected on heating.

measurement within this temperature region in the literature. Large Wilson ratios have been reported for other Rh^{4+} containing compounds, such as the 4H and 6H forms of $BaRhO_3$ as well as the related Rh^{4+} pyrochlore $Lu_2Rh_2O_7$ ($R_w = 1.89, 2.69$ and 2.5 respectively).^(38, 78) In all these compounds the Rh^{4+} cations form a geometrically frustrated lattice, being either a layered 2D Kagome lattice in the case of the $BaRhO_3$ hexagonal perovskites or a 3D tetrahedral arrangement in the pyrochlores. A large Wilson ratio and electron localisation are consistent with the temperature dependence of electrical resistivity shown in Figure 8 which shows relatively high residual resistivity at low temperature. It is possible to fit the high temperature resistivity to an activated form as shown, but this does not persist to low temperatures and is inconsistent with the γ value from heat capacity. This suggests that the behaviour is dominated by grain boundary effects, a suggestion that is supported by the low band gap value determined from the fit. 6H $BaRhO_3$ and $Lu_2Rh_2O_7$ are also reported to show increasing resistivity with decreasing temperatures, of a similar magnitude to $Y_2Rh_2O_7$. In these examples no indication of AFM ordering is present, with all showing Pauli-type paramagnetism. Long range AFM order as well as a high Wilson ratio of approximately 5 is observed in $FeCrAs$ in which the magnetic cations form a 2D Kagome lattice.⁽⁷⁹⁾ A very high Wilson ratio may therefore be correlated to the percolation of AFM order in materials with an inherently geometrically frustrated arrangement of magnetic cations.

Electronic Structures of $Pb_2Rh_2O_7$ and $Y_2Rh_2O_7$ via DFT:

DFT calculations of the band structure and density of states were performed to further elucidate the electronic properties of these materials. Initial calculations assumed a spin-polarised antiferromagnetic arrangement of Rh in the four Rh atom primitive unit cell. Despite the use of a Hubbard U parameter,

stable moments were not found. Accordingly, the results shown are for the non-spin-polarised case. The calculated band structures and density of states are shown in Figure 9 for $Pb_2Rh_2O_7$ and $Y_2Rh_2O_7$. Band structure calculations for $Pb_2Rh_2O_7$ indicate a direct band gap of 0.62 eV for calculations using the experimentally derived structural model while a relaxed structure indicates a bandgap 0.48 eV using GGA and 0.70 eV using GGA+U. We note that the semiconducting gap is consistent with Sleight's report of $Pb_2Rh_2O_7$.⁽⁶⁶⁾ The existence of comparable gaps both with and without the Hubbard U means that the predicted insulating gaps are not due to strong correlation effects, but rather are a consequence of band structure. Secondly, it is important to emphasise that the band gaps are not a consequence of moments on the Rh, since the result emerges without Rh moments. The similar band structures for the Pb and Y compounds imply a similar valence for Rh in the two materials. This result would suggest a Pb valence state differing from Pb^{2+} . In the pyrochlore structure, Rh has an octahedral nearest neighbour environment, which would imply a crystal field splitting into t_{2g} and e_g sub-orbitals, with the five d electrons of Rh^{4+} partially filling the six states in the t_{2g} manifold. However, the site symmetry is reduced from cubic in the pyrochlore lattice, and beyond nearest-neighbour interactions, can be important due to the strong deviation of the metal–O–metal bonds from 180° . There is a split off set of bands of mixed character that form the conduction band. This is the origin of the band gap that we find. The band structure results also provide insight into the Pb configuration. Pb 6s derived bands are found from approximately -9 eV and -7 eV with respect to the valence band maximum. This would seemingly imply Pb^{2+} . However, these bands are derived from hybridised Pb 6s and O 2p orbitals. The four conduction bands between the conduction band minimum and approximately 2 eV also have strongly mixed Pb 6s and O 2p character, with an exceptionally strong Pb 6s character. This would indicate a strong covalent Pb 6s to O 2p bonding; which is also supported by the crystal structure. We find after relaxing the internal coordinates that the Pb has exceptionally short bonds with neighbouring O. Specifically, the eight-fold coordination of Pb has two short Pb–O bonds at 2.19 Å and six longer bonds at 2.54 Å. We note that the sum of the Shannon ionic radii for Pb^{2+} and O^{2-} is 2.67 Å, while with Pb^{4+} it is 2.32 Å, in both cases much longer than the short Pb–O distances. This is indicative of a covalent Pb–O interaction, consistent with the splitting of the Pb 6s states between the deep valence and conduction bands. Thus, we conclude that there is a strong covalency between Pb and O involving the Pb 6s orbitals, explaining the Rh^{4+} observed, consistent with the experimental results. This does not explain, however, the experimental evidence for metallicity. One possible explanation is in terms of disorder, which might donate carriers. This is consistent with the metallic properties observed in other Pb containing pyrochlores.^(80, 81) The calculated bandgap for $Y_2Rh_2O_7$ is 1.7 eV, which is a value that is of interest for various opto-electronic applications. $Pb_2Rh_2O_7$ possesses a smaller band gap compared to $Y_2Rh_2O_7$. This difference arises due to the hybridisation between the Pb 6s and O 2p orbitals at the lower end of the conduction band. Such behaviour is a

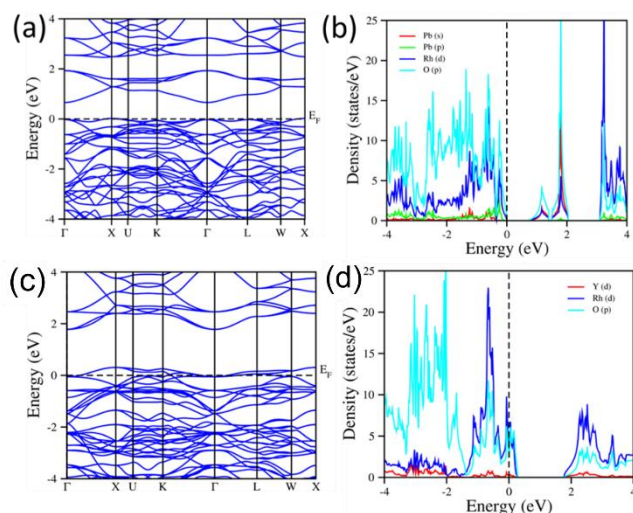


Figure 9: (a) and (c) show the calculated band structures of $\text{Pb}_2\text{Rh}_2\text{O}_7$ and $\text{Y}_2\text{Rh}_2\text{O}_7$ calculated for nonmagnetic ground states using the experimental structures. The bandgap, $E_g = 0.62$ eV. Relaxation using GGA indicates a bandgap of $E_g = 0.48$ eV and GGA+U with a bandgap of $E_g = 0.70$ eV for $\text{Pb}_2\text{Rh}_2\text{O}_7$. The top of the valence band is at 0.29 eV with a large gap at higher energies for $\text{Y}_2\text{Rh}_2\text{O}_7$. Calculated partial density of states are shown in (b) and (d)

commonly observed phenomenon in oxides that contains lead, consistently resulting in a smaller band gap compared to isomorphous compounds without Pb.⁽⁸²⁾ $\text{Y}_2\text{Rh}_2\text{O}_7$, however, is found to be metallic with calculations performed similarly. This emphasises the difference between Pb and Y, reflecting the different chemistry and covalency of Pb with O, which is not expected for Y.

Conclusions

We have successfully synthesised the two new Rh^{4+} containing pyrochlore oxides $\text{Pb}_2\text{Rh}_2\text{O}_7$ and $\text{Y}_2\text{Rh}_2\text{O}_7$ under high pressure, high temperature conditions. The presence of a pure Rh^{4+} state and full oxygen stoichiometry was confirmed by thermogravimetric, spectroscopic, and diffraction techniques. Although the bond valence sums suggest the presence of the unknown Pb^{3+} state, XPS shows there is an approximately equal molar mixture of Pb^{2+} and Pb^{4+} . There is no evidence of the ordering of these cations from the diffraction experiments. $\text{Y}_2\text{Rh}_2\text{O}_7$ presents a unique case where the lower density pyrochlore structure is stabilised under high-pressure conditions, instead of the associated higher density perovskite YRhO_3 . This is a result of the ability for high synthesis pressures to stabilise the Rh^{4+} state in these metastable materials. Catalytic results do not show any trend dependent upon Rh oxidation state but suggest interesting paths for further investigation on the influence of the Rh pyrochlore structural features towards OER activity. The physical properties of $\text{Pb}_2\text{Rh}_2\text{O}_7$ are consistent with other $\text{Pb}_2\text{M}_2\text{O}_7$ pyrochlores where metallic paramagnetism is observed. For $\text{Y}_2\text{Rh}_2\text{O}_7$ a large Wilson ratio indicates a highly correlated system defined by the coexistence of metallic-like conductivity with AFM coupling. An unusual temperature dependence of resistivity is observed, similar to the metallic nonmetal $\text{Lu}_2\text{Rh}_2\text{O}_7$.⁽⁷⁸⁾ Further

investigation into Rh^{4+} containing materials, which have been shown to be reliably synthesised under HPHT conditions is warranted in order to better understand these competing electron localisation and delocalisation effects.

Author Contributions

The project was conceived by Sean D. Injac who undertook the synthesis and initial structural characterisation via XRD measurements and bulk DC magnetization measurements under the supervision of Yuichi Shimakawa. Catalytic measurements, XPS measurements, and discussion were undertaken by Bryce Mullens, Alex Yuen and Christopher Barnett under the supervision of Brenden Kennedy. Magnetic and electronic transport measurements were undertaken by Sean Injac and Fabio Denis Romero. Synchrotron measurements were undertaken by Midori Amano Patino. Neutron powder diffraction measurements were undertaken by Maxim Avdeev. Supratik Mukherjee performed Density Functional calculations with VASP under the supervision of G. Vaitheeswaran. David Singh did density functional calculations with the WIEN2k code and interpreted results.

Conflicts of interest

There are no conflicts to declare.

Acknowledgements

The work was partly supported by Grants-in-Aid for Scientific Research (Nos. 19H05823, 20K20547, 20H00397, 22KK0075, and 23H05457) from MEXT of Japan, and Advanced International Collaborative Research (AdCORP) Grant No. JPMJKB2304 by Japan Science and Technology Agency. Brendan J Kennedy and Alex Yuen acknowledge the support of the Australian Research Council for this work that was facilitated by access to Sydney Analytical, a core research facility at the University of Sydney and was in part undertaken at the Australian Centre for Neutron Scattering. Bryce G. Mullens thanks the Australian Institute for Nuclear Science and Engineering for a PGRA scholarship. Supratik Mukherjee is thankful to DRDO, India, via ACRHEM (DRDO/18/1801/2016/01038: ACRHEM-PHASE-III) for the financial support, and CMSD, University of Hyderabad, for providing computational facilities. G. Vaitheeswaran would like to acknowledge the Institute of Eminence, University of Hyderabad (UoH-IoE-RC3-21-046) for funding.

Notes and references

- Subramanian MA, Aravamudan G, Subba Rao GV. Oxide pyrochlores — A review. *Progress in Solid State Chemistry*. 1983;15(2):55-143.
- Kim J, Shih P-C, Tsao K-C, Pan Y-T, Yin X, Sun C-J, et al. High-performance pyrochlore-type yttrium ruthenate electrocatalyst for oxygen evolution reaction in acidic media. *Journal of the American Chemical Society*. 2017;139(34):12076-83.

3. Anantharaman AP, Dasari HP. Potential of pyrochlore structure materials in solid oxide fuel cell applications. *Ceramics International*. 2021;47(4).
4. Weller T, Specht L, Marschall R. Single crystal CsTaWO₆ nanoparticles for photocatalytic hydrogen production. *Nano Energy*. 2017;31:551-9.
5. Hallas AM, Arevalo-Lopez AM, Sharma AZ, Munsie T, Attfield JP, Wiebe CR, et al. Magnetic frustration in lead pyrochlores. *Physical Review B*. 2015;91(10):104417.
6. Hiroi Z, Yonezawa S, Muraoka Y. Unprecedented superconductivity in beta-pyrochlore osmate KOs₂O₆. *Journal of the Physical Society of Japan*. 2004;73(7):1651-4.
7. Dun ZL, Lee M, Choi ES, Hallas AM, Wiebe CR, Gardner JS, et al. Chemical pressure effects on magnetism in the quantum spin liquid candidates Yb₂X₂O₇ (X=Sn, Ti, Ge). *Physical Review B*. 2014;89(6):064401.
8. Subramanian MA, Torardi CC, Johnson DC, Pannetier J, Sleight AW. Ferromagnetic R₂Mn₂O₇ pyrochlores (R = Dy, Lu, Y). *Journal of Solid State Chemistry*. 1988;72(1):24-30.
9. Harris MJ, Bramwell S, McMorro D, Zeiske T, Godfrey K. Geometrical frustration in the ferromagnetic pyrochlore Ho₂Ti₂O₇. *Physical Review Letters*. 1997;79(13):2554.
10. Lebedev D, Povia M, Waltar K, Abdala PM, Castelli IE, Fabbri E, et al. Highly Active and Stable Iridium Pyrochlores for Oxygen Evolution Reaction. *Chemistry of Materials*. 2017;29(12):5182-91.
11. Sardar K, Petrucco E, Hiley CI, Sharman JDB, Wells PP, Russell AE, et al. Water-Splitting Electrocatalysis in Acid Conditions Using Ruthenate-Iridate Pyrochlores. *Angewandte Chemie-International Edition*. 2014;53(41):10960-4.
12. Avdeev M, Haas MK, Jorgensen JD, Cava RJ. Static disorder from lone-pair electrons in Bi_{2-x}MxRu₂O_{7-y} (M=Cu,Co;x=0,0.4) pyrochlores. *Journal of Solid State Chemistry*. 2002;169(1):24-34.
13. Kim M, Ju H, Kim J. Single crystalline Bi₂Ru₂O₇ pyrochlore oxide nanoparticles as efficient bifunctional oxygen electrocatalyst for hybrid Na-air batteries. *Chemical Engineering Journal*. 2019;358:11-9.
14. Takeda T, Nagata M, Kobayashi H, Kanno R, Kawamoto Y, Takano M, et al. High-Pressure Synthesis, Crystal Structure, and Metal-Semiconductor Transitions in the Tl₂Ru₂O_{7-δ} Pyrochlore. *Journal of Solid State Chemistry*. 1998;140(2):182-93.
15. Wang R, Sleight AW. Synthesis and characterization of Cd₂Ru₂O₇. *Materials Research Bulletin*. 1998;33(7):1005-7.
16. Kanno R, Takeda Y, Yamamoto T, Kawamoto Y, Yamamoto O. Crystal Structure and Electrical Properties of the Pyrochlore Ruthenate Bi_{2-x}YxRu₂O₇. *Journal of Solid State Chemistry*. 1993;102(1):106-14.
17. Field M, Kennedy BJ, Hunter BA. Structural Studies of the Metal-Nonmetal Transition in Ru Pyrochlores. *Journal of Solid State Chemistry*. 2000;151(1):25-30.
18. Yamamoto T, Kanno R, Takeda Y, Yamamoto O, Kawamoto Y, Takano M. Crystal Structure and Metal-Semiconductor Transition of the Bi_{2-x}Ln_xRu₂O₇ Pyrochlores (Ln = Pr-Lu). *Journal of Solid State Chemistry*. 1994;109(2):372-83.
19. Kennedy BJ, Vogt T. Structural and Bonding Trends in Ruthenium Pyrochlores. *Journal of Solid State Chemistry*. 1996;126(2):261-70.
20. Kobayashi H, Kanno R, Kawamoto Y, Kamiyama T, Izumi F, Sleight AW. Synthesis, Crystal Structure, and Electrical Properties of the Pyrochlores Pb_{2-x}Ln_xRu₂O_{7-y} (Ln = Nd, Gd). *Journal of Solid State Chemistry*. 1995;114(1):15-23.
21. Kennedy BJ. Structure refinement of Y₂Ru₂O₇ by neutron powder diffraction. *Acta Crystallographica Section C: Crystal Structure Communications*. 1995;51(5):790-2.
22. Reading J, Knee CS, Weller MT. Syntheses, structures and properties of some osmates(IV,V) adopting the pyrochlore and weberite structures. *Journal of Materials Chemistry*. 2002;12(8):2376-82.
23. Das M, Bhowal S, Sannigrahi J, Bandyopadhyay A, Banerjee A, Cibir G, et al. Interplay between structural, magnetic, and electronic states in the pyrochlore iridate Eu₂Ir₂O₇. *Physical Review B*. 2022;105(13):134421.
24. Jacobsen H, Dashwood CD, Lhotel E, Khalyavin D, Manuel P, Stewart R, et al. Strong quantum fluctuations from competition between magnetic phases in a pyrochlore iridate. *Physical Review B*. 2020;101(10):104404.
25. Guo H, Ritter C, Komarek AC. Direct determination of the spin structure of Nd₂Ir₂O₇ by means of neutron diffraction. *Physical Review B*. 2016;94(16):161102.
26. Lefrançois E, Cathelin V, Lhotel E, Robert J, Lejay P, Colin CV, et al. Fragmentation in spin ice from magnetic charge injection. *Nature Communications*. 2017;8(1):209.
27. Cathelin V, Lefrançois E, Robert J, Guruciaga PC, Paulsen C, Prabhakaran D, et al. Fragmented monopole crystal, dimer entropy, and Coulomb interactions in Dy₂Ir₂O₇. *Physical Review Research*. 2020;2(3):032073.
28. Kim M, Ju H, Kim J. Highly efficient bifunctional catalytic activity of bismuth rhodium oxide pyrochlore through tuning the covalent character for rechargeable aqueous Na-air batteries. *Journal of Materials Chemistry A*. 2018;6(18):8523-30.
29. Shih P-C, Kim J, Sun C-J, Yang H. Single-Phase Pyrochlore Y₂Ir₂O₇ Electrocatalyst on the Activity of Oxygen Evolution Reaction. *ACS Applied Energy Materials*. 2018;1(8):3992-8.
30. Kim M, Ju H, Kim J. Single crystalline thallium rhodium oxide pyrochlore for highly improved round trip efficiency of hybrid Na-air batteries. *Dalton Transactions*. 2018;47(42):15217-25.
31. Kiss B, Didier C, Johnson T, Manning TD, Dyer MS, Cowan AJ, et al. Photocatalytic water oxidation by a pyrochlore oxide upon irradiation with visible light: rhodium substitution into yttrium titanate. *Angewandte Chemie*. 2014;126(52):14708-12.
32. Pakhare D, Schwartz V, Abdelsayed V, Haynes D, Shekhawat D, Poston J, et al. Kinetic and mechanistic study of dry (CO₂) reforming of methane over Rh-substituted La₂Zr₂O₇ pyrochlores. *Journal of Catalysis*. 2014;316:78-92.
33. Wu J, Qiao LY, Zhou ZF, Cui GJ, Zong SS, Xu DJ, et al. Revealing the Synergistic Effects of Rh and Substituted La₂B₂O₇ (B = Zr or Ti) for Preserving the Reactivity of Catalyst in Dry Reforming of Methane. *Acs Catalysis*. 2019;9(2):932-45.
34. Stitzer KE, Smith MD, Darriet J, Loye HCz. Crystal growth, structure determination and magnetism of a new hexagonal rhodate: Ba₉Rh₈O₂₄. *Chemical Communications*. 2001(17):1680-1.
35. Stitzer KE, El Abed A, Darriet J, zur Loye H-C. Crystal Growth and Structure Determination of Barium Rhodates: Stepping Stones toward 2H-BaRhO₃. *Journal of the American Chemical Society*. 2004;126(3):856-64.
36. Chamberland BL, Anderson JB. The preparation and crystal structure of a BaRhO₃ polytype. *Journal of Solid State Chemistry*. 1981;39(1):114-9.
37. Siegrist T, Larson EM, Chamberland BL. Structural studies of high-pressure Ba · Rh · O phases. *Journal of Alloys and Compounds*. 1994;210(1):13-7.
38. Injac SD, Xu Y, Romero FD, Shimakawa Y. Pauli-paramagnetic and metallic properties of high pressure polymorphs of BaRhO₃ oxides containing Rh₂O₉ dimers. *Dalton Transactions*. 2021;50(13):4673-9.

39. Avdeev M, Hester JR. ECHIDNA: a decade of high-resolution neutron powder diffraction at OPAL. *Journal of Applied Crystallography*. 2018;51(6):1597-604.
40. Kresse G, Furthmüller J. Efficiency of ab-initio total energy calculations for metals and semiconductors using a plane-wave basis set. *Computational materials science*. 1996;6(1):15-50.
41. Kresse G, Furthmüller J. Efficient iterative schemes for ab initio total-energy calculations using a plane-wave basis set. *Physical review B*. 1996;54(16):11169.
42. Kresse G, Joubert D. From ultrasoft pseudopotentials to the projector augmented-wave method. *Physical review b*. 1999;59(3):1758.
43. Perdew JP, Burke K, Ernzerhof M. Generalized gradient approximation made simple. *Physical review letters*. 1996;77(18):3865.
44. Monkhorst HJ, Pack JD. Special points for Brillouin-zone integrations. *Physical review B*. 1976;13(12):5188.
45. Liechtenstein A, Anisimov VI, Zaanen J. Density-functional theory and strong interactions: Orbital ordering in Mott-Hubbard insulators. *Physical Review B*. 1995;52(8):R5467.
46. Krukau AV, Vydrov OA, Izmaylov AF, Scuseria GE. Influence of the exchange screening parameter on the performance of screened hybrid functionals. *The Journal of chemical physics*. 2006;125(22).
47. Ouahrani T, Boufatah RM, Benaissa M, Morales-García Á, Badawi M, Errandonea D. Effect of intrinsic point defects on the catalytic and electronic properties of Cu₂WS₄ single layer: Ab initio calculations. *Physical Review Materials*. 2023;7(2):025403.
48. Janthon P, Luo S, Kozlov SM, Vines F, Limtrakul J, Truhlar DG, et al. Bulk properties of transition metals: a challenge for the design of universal density functionals. *Journal of chemical theory and computation*. 2014;10(9):3832-9.
49. Fu Y, Singh DJ. Density functional methods for the magnetism of transition metals: SCAN in relation to other functionals. *Physical Review B*. 2019;100(4):045126.
50. Blaha P, Schwarz K, Tran F, Laskowski R, Madsen GK, Marks LD. WIEN2k: An APW+lo program for calculating the properties of solids. *The Journal of chemical physics*. 2020;152(7).
51. Shirako Y, Wang X, Tsujimoto Y, Tanaka K, Guo Y, Matsushita Y, et al. Synthesis, Crystal Structure, and Electronic Properties of High-Pressure PdF₂-Type Oxides MO₂ (M = Ru, Rh, Os, Ir, Pt). *Inorganic Chemistry*. 2014;53(21):11616-25.
52. Banerjee A, Singh Z. Determination of thermodynamic properties of YRhO₃(s) by solid-state electrochemical cell and differential scanning calorimeter. *Journal of Solid State Electrochemistry*. 2010;14(7):1227-33.
53. Beyerlein RA, Horowitz HS, Longo JM, Leonowicz ME, Jorgensen JD, Rotella FJ. Neutron diffraction investigation of ordered oxygen vacancies in the defect pyrochlores, Pb₂Ru₂O_{6.5} and PbTiNb₂O_{6.5}. *Journal of Solid State Chemistry*. 1984;51(2):253-65.
54. Akazawa T, Inaguma Y, Katsumata T, Hiraki K, Takahashi T. Flux growth and physical properties of pyrochlore Pb₂Ru₂O_{6.5} single crystals. *Journal of Crystal Growth*. 2004;271(3):445-9.
55. Kennedy BJ. Oxygen Vacancies in Pyrochlore Oxides: Powder Neutron Diffraction Study of Pb₂Ir₂O_{6.5} and Bi₂Ir₂O_{7-y}. *Journal of Solid State Chemistry*. 1996;123(1):14-20.
56. Birch F. Finite elastic strain of cubic crystals. *Physical review*. 1947;71(11):809.
57. Kumar RS, Cornelius AL, Somayazulu M, Errandonea D, Nicol MF, Gardner J. High pressure structure of Tb₂Ti₂O₇ pyrochlore at cryogenic temperatures. *physica status solidi (b)*. 2007;244(1):266-9.
58. Srihari V, Verma AK, Pandey KK, Vishwanadh B, Panchal V, Garg N, et al. Making Yb₂Hf₂O₇ defect fluorite incompressible by particle size reduction. *The Journal of Physical Chemistry C*. 2021;125(49):27354-62.
59. Shaplygin I.S. PII, Lazarev V.B. The Chemistry and Properties of Complex Oxides of Rhodium. *Russ J Inorg Chem (Engl Transl)*. 1986;31:1649.
60. Cheng J-G, Kweon KE, Zhou J-S, Alonso JA, Kong P-P, Liu Y, et al. Anomalous perovskite PbRuO₃ stabilized under high pressure. *Proceedings of the National Academy of Sciences*. 2013;110(50):20003-7.
61. Denis Romero F, Amano Patino M, Haruta M, Kurata H, Attfield JP, Shimakawa Y. Conversion of a Defect Pyrochlore into a Double Perovskite via High-Pressure, High-Temperature Reduction of Te⁶⁺. *Inorganic Chemistry*. 2020;59(1):343-9.
62. Jin C-Q, Zhou J-S, Goodenough J, Liu Q, Zhao J, Yang L, et al. High-pressure synthesis of the cubic perovskite BaRuO₃ and evolution of ferromagnetism in ARuO₃ (A= Ca, Sr, Ba) ruthenates. *Proceedings of the National Academy of Sciences*. 2008;105(20):7115-9.
63. Gibbs AS, Knight KS, Lightfoot P. High-temperature phase transitions of hexagonal YMnO₃. *Physical Review B*. 2011;83(9):094111.
64. Yamaura K, Huang Q, Young DP, Noguchi Y, Takayama-Muromachi E. Crystal structure and electronic and magnetic properties of the bilayered rhodium oxide Sr₃Rh₂O₇. *Physical Review B*. 2002;66(13):134431.
65. Ismunandar, Kennedy BJ, Hunter BA. Phase transformation in CuRh₂O₄: a powder neutron diffraction study. *Materials Research Bulletin*. 1999;34(1):135-43.
66. Sleight AW. High pressure synthesis of platinum metal pyrochlores of the type Pb₂M₂O_{6-δ}. *Materials Research Bulletin*. 1971;6(8):775-80.
67. Thomas JM, Tricker MJ. Electronic structure of the oxides of lead. Part 2.—An XPS study of bulk rhombic PbO, tetragonal PbO, β-PbO₂ and Pb₃O₄. *Journal of the Chemical Society, Faraday Transactions 2: Molecular and Chemical Physics*. 1975;71:329-36.
68. Payne DJ, Egdell RG, Hao W, Foord JS, Walsh A, Watson GW. Why is lead dioxide metallic? *Chemical Physics Letters*. 2005;411(1-3):181-5.
69. Payne DJ, Egdell RG, Law DS, Glans P-A, Learmonth T, Smith KE, et al. Experimental and theoretical study of the electronic structures of α-PbO and β-PbO₂. *Journal of Materials Chemistry*. 2007;17(3):267-77.
70. Kövér L, Tóth J, Itoh A. An experimental method for resolution calibration of electron spectrometers. *Acta Physica Hungarica*. 1989;65(2-3):217-23.
71. Abe Y, Kato K, Kawamura M, Sasaki K. Rhodium and rhodium oxide thin films characterized by XPS. *Surface Science Spectra*. 2001;8(2):117-25.
72. McCrory CCL, Jung S, Peters JC, Jaramillo TF. Benchmarking Heterogeneous Electrocatalysts for the Oxygen Evolution Reaction. *Journal of the American Chemical Society*. 2013;135(45):16977-87.
73. Khan MS, Carlomagno I, Meneghini C, Biswas P, Bert F, Majumdar S, et al. Mixed-valent metallic pyrochlore iridate: A possible route to non-Fermi liquids. *Physical Review B*. 2022;105(8):085137.
74. Battle PD, Frost JR, Kim S-H. Magnetic properties of La₂CuTi_{1-x}Ru_xO₆ and La₂ZnRuO₆. *Journal of Materials Chemistry*. 1995;5(7):1003-6.
75. Yamaura K, Shirako Y, Kojitani H, Arai M, Young DP, Akaogi M, et al. Synthesis and magnetic and charge-transport properties of the correlated 4d post-perovskite CaRhO₃. *Journal of the American Chemical Society*. 2009;131(7):2722-6.

76. Taira N, Wakeshima M, Hinatsu Y. Magnetic Properties of Ruthenium Pyrochlores $Y_2Ru_2O_7$ and $Lu_2Ru_2O_7$. *Journal of Solid State Chemistry*. 1999;144(1):216-9.
77. Greedan JE. Frustrated rare earth magnetism: Spin glasses, spin liquids and spin ices in pyrochlore oxides. *Journal of Alloys and Compounds*. 2006;408:444-55.
78. Hallas AM, Sharma AZ, Mauws C, Chen Q, Zhou HD, Ding C, et al. Coexistence of metallic and nonmetallic properties in the pyrochlore $Lu_2Rh_2O_7$. *npj Quantum Materials*. 2019;4(1):9.
79. Wu W, McCollam A, Swainson I, Rourke PMC, Rancourt DG, Julian SR. A novel non-Fermi-liquid state in the iron-pnictide $FeCrAs$. *Europhysics Letters*. 2009;85(1):17009.
80. Cox PA, Egdell RG, Goodenough JB, Hamnett A, Naish CC. The metal-to-semiconductor transition in ternary ruthenium(IV) oxides - a study by electron-spectroscopy. *Journal of Physics C-Solid State Physics*. 1983;16(32):6221-39.
81. Khan MS, Carlomagno I, Meneghini C, Biswas PK, Bert F, Majumdar S, et al. Mixed-valent metallic pyrochlore iridate: A possible route to non-Fermi liquids. *Physical Review B*. 2022;105(8):085137.
82. Monteseuro V, Ruiz-Fuertes J, Contreras-García J, Rodríguez-Hernández P, Muñoz A, Errandonea D. High pressure theoretical and experimental analysis of the bandgap of $BaMoO_4$, $PbMoO_4$, and $CdMoO_4$. *Applied Physics Letters*. 2019;115(1).